metals

MDPI

Article

Fe_3O_4 Coated SiO_2 Magnetic Nanoparticles for Enhanced Antibacterial Activity and Electrochemical Sensing

Madhavi [1], Mukesh Kumar [1,*], Jamilur R. Ansari [2], Vinay Kumar [3], Sushil Nagar [4] and Ashutosh Sharma [4,5,*]

[1] Department of Physics, Faculty of Science, Shree Guru Gobind Singh Tricentenary University, Gurgaon 122505, Delhi-NCR, India
[2] Department of Applied Science, Laxmi Devi Institute of Engineering & Technology, Alwar-Tijara-Delhi Highway, Chikani, Alwar 301028, Rajasthan, India
[3] Department of Physics, COBS&H, CCS Haryana Agricultural University, Hisar 125004, Haryana, India
[4] Department of Bio-Chemistry, COBS&H, CCS Haryana Agricultural University, Hisar 125004, Haryana, India
[5] Department of Materials Science and Engineering, Ajou University, Suwon 16499, Republic of Korea
* Correspondence: mukesh.kumar@sgtuniversity.org (M.K.); ashu.materials@gmail.com (A.S.); Tel.: +91-9646496952 (M.K.); +82-1095345040 (A.S.)

Abstract: Multifunctional magnetic composite nanoparticles (NPs) with antibiotics have demonstrated symbiotic effects because of their promising antimicrobial properties. The antimicrobial agent reduces side effects and dosage, and increases drug delivery efficiency. In this study, SiO_2 coated over Fe_3O_4 magnetic nanoparticles (MNPs) were prepared by a solvothermal method. The MNPs were characterized by using X-ray diffraction (XRD), transmission electron microscopy (TEM), ultraviolet-visible spectroscopy (UV-vis), and Fourier transform infrared spectroscopy (FTIR). The antimicrobial tests were carried out using the disk diffusion method. The electrochemical sensing was investigated by cyclic voltammetry with varying As(III) concentrations from 1–10 ppb. The microstructural results showed the formation of spherical-shaped Fe_3O_4@SiO_2 MNPs with 15–30 nm diameters. UV-vis results showed that Fe_3O_4 NPs promote visible light absorption of Fe_3O_4@SiO_2 MNPs because of well-structured and unvarying shell thickness which is beneficial for the absorption of organic dyes. With an increase in the concentration of As(III), there was a shift in potential and an increase in oxidation peak current, showing the electrocatalytic capacity of the modified electrode. The SiO_2 deposited on Fe_3O_4 displayed an admirable microbial operation. These Fe_3O_4@SiO_2 MNPs are easily absorbed by cells and have the potential to influence bacterial cells both within and outside of the cell membrane, making them an intriguing candidate for use in a variety of biological applications in the future.

Keywords: Fe_3O_4@SiO_2 MNPs; magnetic nanoparticles; antibacterial; biomedical; Arsenic (III)

Citation: Madhavi; Kumar, M.; Ansari, J.R.; Kumar, V.; Nagar, S.; Sharma, A. Fe_3O_4 Coated SiO_2 Magnetic Nanoparticles for Enhanced Antibacterial Activity and Electrochemical Sensing. *Metals* **2022**, *12*, 2145. https://doi.org/10.3390/met12122145

Academic Editor: Leonid M. Kustov

Received: 21 November 2022
Accepted: 9 December 2022
Published: 14 December 2022

1. Introduction

The increased risk of bacterial infections is a serious issue for public health, extensively, which decreases the regulation of standard antibiotics in the body and importantly increases clinical complications [1,2]. The death rate has increased to 25% in the world gradually. Therefore, antibiotics have been used rigorously to cure bacterial infections [3,4]. Some examples of antibiotics used are ampicillin, nystatin, and amphotericin. Contrary to how antibiotics like ampicillin impact the kidney, neurological system, and blood, nystatin is hydrophobic and prevents microbial infections. Therefore, to achieve the maximum benefit of antibiotics, increasing drug efficiency is vital for cellular growth. New antibacterial agents produced using nanomaterials have been developed in the past. Nanoparticles (NPs) have unique properties such as surface-to-volume ratios, and different physical–chemical and biological properties, and also provide wider usage in biomedical applications [5–7]. Popular iron oxide MNPs are highly susceptible to aggregation within the cellular environment. Thus, to protect from the aggregation of iron oxide NPs, various noble metal and

oxide (Au, Ag, SiO_2, etc.) NPs have been coated over iron oxide NPs. The type of coating generally depends on the application. The right coating enables MNPs to target particular areas while remaining non-toxic. In the last decades, there have been many nanomaterials used as antibacterial agents such as Ag [7–10], Cu [11], Au [12,13], ZnO_2 [14], SiO_2 [15], and graphene oxide [16,17]. Among all of these, SiO_2 is the most exceptional antibacterial agent due to its high toxicity for microorganisms and low toxicity for human beings.

In addition, the most significant transition metal oxides with various technological implications are iron oxides. Various kinds of iron oxide polymorphs can be found in the natural world. The most prevalent polymorphs of iron oxides are hematite (α-Fe_2O_3), magnetite (Fe_3O_4), and maghemite (Y-Fe_2O_3) [18]. Magnetite Fe_3O_4 is the most fascinating of all iron oxides due to the presence of iron cations in two valence states, Fe^{3+} and Fe^{2+}, in the inverse spinel structure. The cubic spinel Fe_3O_4 exhibits ferromagnetism below 585 °C [19]. However, two significant problems with magnetite NPs include fast agglomeration and oxidation by airborne oxygen. The most popular method of surface modification for conjugating organic or inorganic molecules to iron oxide nanoparticle (IONPs) surfaces is coating. This technique not only keeps IONPs from oxidizing and clumping together, but it also offers the chance for additional functionalization [20].

Around the world, heavy metals are a major cause of groundwater pollution where arsenic (As), one of these heavy metals, is a major factor in several illnesses. Skin lesions, skin cancer, Blackfoot disease, and ventricular fibrillation are a few examples of such skin disorders impacting many countries, e.g., Poland, Argentina, Chile, Vietnam, Cambodia, Malaysia, Taiwan, India, and Bangladesh [21]. Unfortunately, many of these places in Southeast Asia are underdeveloped and lack the resources to combat these issues. On these grounds, it becomes essential to choose a material with dual bactericidal mechanisms. In other words, the co-existence of Fe_3O_4 and SiO_2 NPs can activate antimicrobial as well as sensing mechanisms simultaneously which eventually lead to the development of a better antimicrobial behavior under visible light irradiation, seeming consistent with an earlier investigation on TiO_2-CuO NPs [22]. Both Fe_3O_4 and SiO_2 have been used in antibacterial and sensing mechanisms [23,24]. Due to this, it is necessary to evaluate the sensing performance of Fe_3O_4@SiO_2 using As(III) [25].

In this present work, SiO_2 is coated over Fe_3O_4 to protect from antibacterial growth. The Fe_3O_4@SiO_2 MNPs with a diameter of less than 20 nm have shown reduced antibacterial activity [21]. After coating with SiO_2, the properties of Fe_3O_4 change and it demonstrates chemical surface modifiability and low cytotoxicity [26]. Recent studies show the importance of active sites in the surface functionalization of MNPs. Qu et al. designed symmetric NiP_1N_3 atomic active sites for the electrochemical reduction of CO [27]. Recently, Huo et al. have synthesized $Fe_{36}Co_{44}$ bimetallic nanoclusters for catalytic hydrolysis of ammonia borane [28]. The surface of the SiO_2 shell at the Fe_3O_4 particle core provides the active sites for the attachment of bacteria. The catalytic active sites in the Fe_3O_4@SiO_2 MNPs are Fe^{+3}. This Fe^{3+} ion possesses a Lewis acid character that further promotes surface modification with functional groups, bacteria, and other derivatives to demonstrate surface activity and antibacterial properties [29]. The Fe_3O_4@SiO_2 MNPs have a lower ability to eliminate Gram-positive bacteria than Gram-negative bacteria which is related to the strength of SiO_2 NPs opposing the microbial membranes. This stable nature of SiO_2 increases the difficulty in penetrating the Fe_3O_4 membrane for microbial activity [5,30,31]. Moreover, the main cause of human death is Gram-positive bacteria. The assemblage of SiO_2 coating becomes an impediment to antibacterial growth. Silica is the most auspicious and advantageous coating material, because it protects MNPs from agglomeration and oxidation at diverse pH values, improving chemical stability. Thus, SiO_2 has imperative properties, such as good compatibility, and hydrophilicity favors biomedical application [32]. SiO_2 has been frequently employed as a coating for magnetic nanoparticles because of its biocompatibility, nontoxicity, chemical inertness, extremely high specific surface area with many Si-OH bonds on the surface, non-magnetic characteristics, and biostability [33,34]. Since environmentally friendly technologies might lessen biological

threats to living cells, they can be advantageous for the production of nano-antibacterial compounds [35]. Recently, several in-situ fabrication techniques were created in order to get rid of harmful reducing agents such as KBH_4 and hydrazine from the final system. Ag nanoparticles of various sizes and coverage were coated onto the surface of PS/PDA microspheres by leveraging the reducing property of polydopamine (PDA), and the resulting antibacterial agent displayed improved performance against *Escherichia coli* and *Staphylococcus aureus* [30]. The microemulsion method and Stober's method, which involve alkaline hydrolysis of tetraethyl orthosilicate, are now the two main techniques for coating silica onto Fe_3O_4 NPs [18]. Micelles are used in the microemulsion technique to control and contain the coating. It creates core-shell NPs with a surfactant layer on the silica surface, partially negating the benefit of the silica surface's simple bio-conjugations. Contrarily, core-shell Fe_3O_4@SiO_2 NPs without the need for a surfactant might be produced by the alkaline hydrolysis of tetraethyl orthosilicate (TEOS), which is stable and simple to disperse. The core-shell Fe_3O_4@SiO_2 NPs are unquestionably the best model NPs for the finding of bio-applications since they have a pristine silica surface. [14,36].

Recently, Fe_3O_4 MNPs have fascinated researchers because of their most promising magnetic properties, especially for medical applications such as targeted drug delivery, magnetic resonance imaging (MRI), hyperthermia therapeutic agents, and biomolecules separation because of low toxicity, biocompatible and surface-modifiable property [37,38]. Cu-based antimicrobial surfaces are enabling a revival in the fight against the epidemiology of healthcare-associated infections. Several strategies exist to create and change surfaces with superior antibacterial characteristics because of recent improvements in biotechnology and material science methodologies [39,40]. Though there are many other material or elements i.e., Au, Ni, Co, etc., we prefer using iron oxide because it has competitive advantages compared to others. Iron oxide is formed by a chemical combination of iron with oxygen, and it stands as the backbone of the current infrastructure. The synthesis of Fe_3O_4 is easily proceeded by the co-precipitation method using salts of ferric and ferrous under an inert atmosphere, using nitrogen gas keeping pH 12 for the solution. Iron oxide disperses well in a variety of liquid media with varying pH levels [41]. To improve the antimicrobial properties of Fe_3O_4, SiO_2 coatings have been investigated for enhancing their stability and biocompatibility [42]. The surface of the magnetic nanoparticles must be functionalized to increase their biocompatibility [33]. Silica has been utilized extensively as a coating for magnetic nanoparticles because of its biocompatibility, nontoxicity, chemical inertness, extremely high specific surface area with many Si-OH bonds on the surface, non-magnetic characteristics, and biostability [43,44]. One of the most used methods for silica coating is the Stöber synthesis method. The advantages of silica shell include its ease of further functionalization, improved water solubility, protection of the core from oxidation and degradation, increased resistance to highly acidic solutions, and ease of further conjugation with various functional groups. These features make it possible to couple and label bio targets with selectivity and specificity. The bio-toxicity analysis of the nanomagnetic silica-coated (Fe_3O_4@SiO_2) composite shows that it is biocompatible [45]. Fe_3O_4 NPs may therefore make good candidates for their prospective application in antimicrobial therapy. The objective of the current study is to create, characterize, and assess the antibacterial activity of microemulsion-produced Fe_3O_4 and silica-coated Fe_3O_4 MNPs [46]. We report on a modified Stöber approach to creating water-soluble core-shell Fe_3O_4@SiO_2 MNPs without the need for a surfactant in this study [36]. Environmentally friendly techniques are advantageous for creating nano-antibacterial agents since they can lessen the biological risk to cell life [35,47].

2. Experimental

2.1. Materials

Merck provided the tetraethyl orthosilicate (TEOS, 98%) and citric acid trisodium salt dehydrate ($C_6H_5Na_3O_7.2H_2O$, 99%), while Alfa Aesar provided the Ferric chloride hexahydrate ($FeCl_3.6H_2O$, 99%), ammonia hydroxide (25 wt%), ethylene glycol, and ethanol

(99.9%). All the chemicals were of reagent grades. We used all of the chemicals as received without further purification.

2.1.1. Synthesis of Fe_3O_4 MNPs

Using salts of ferrous and ferric under an inert atmosphere created by nitrogen (N2) gas, we were able to create Fe_3O_4 MNPs. In 250 mL of ultra-pure de-oxygenated Millipore water (18.2 MΩ.cm), we varied $FeCl_3$ from 15 to 18 g and $FeCl_2$ from 5–7 g. The combined solution was stirred magnetically for two hours. After adding 2 M NaOH aqueous solution in the presence of N_2 gas, the solution precipitated at room temperature. The process was maintained at 700 °C for six hours with the solution's pH remaining at 12.

According to Sophie et al., the precipitation of Fe_3O_4 was completed as anticipated at pH values ranging between 8 and 14. Following precipitation, the solution was cooled to room temperature, the precipitate was separated using a permanent magnet (2500 Gauss), and the precipitate was repeatedly washed with ultra-pure deoxygenated Millipore water until the pH of the solution was neutral. Finally, we used pure acetone to clean the Fe_3O_4 before drying it at 700 °C in a vacuum oven.

The overall precipitation reaction can be written as follows:

$$Fe^{2+} + 2Fe^{3+} + 8OH^- \leftrightarrow Fe\ (OH)_2 + 2Fe(OH)_3 \rightarrow Fe_3O_4\downarrow + 4H_2O$$

2.1.2. Synthesis of Fe_3O_4@SiO_2 MNPs

According to the Stöber method, core-shell Fe_3O_4@SiO_2 MNPs were created by hydrolyzing tetraethyl orthosilicate (TEOS) in the presence of Fe_3O_4 MNPs [48]. Using a solvothermal coating technique first, ethylene glycol (80 mL) and $FeCl_3.6H_2O$ (3.2 g) were mixed by stirring for 30 min. Anhydrous sodium acetate (4.8 g) was then added to the mixture, and the mixture was stirred for the next 30 min. Yellow citrate (0.8 g) was also added to the solution mixture. After hydrothermal synthesis, the resulting black substance was cleaned and dried. Fe_3O_4 NPs (0.1 g) were dispersed in a water–ethanol mixture in 100:25 ratios to create the Fe_3O_4@SiO_2 structure. Next, $NH_3.H_2O$ (1.5 mL) was added. The entire content was then submerged in an ultrasonic bath for 10 min. Following thorough mixing, 1 cc of TEOS was added, and the mixture was agitated for a further 6 h. The resultant product was then magnetized to separate it from the finished product, and it was then dried for 12 h at 80 °C in a vacuum oven.

3. Characterization

The characterization techniques were utilized to gain a better knowledge of surface chemistry and crystal structure. We employed X-Ray Diffraction (XRD) and UV-vis spectroscopy to study the structural and absorption characteristics of MNPs, respectively. Transmission electron microscopy (TEM) and Fourier transform infrared spectroscopy (FTIR) were also employed to evaluate the structural and absorption properties of MNPs at high resolution. The chemical bonds between the Fe_3O_4 core and the surface covering were revealed by FTIR findings. Finally, we performed antibacterial tests and electrochemical sensing studies. The samples for electron microscopy studies were prepared by ultrasonication of MNPs in ethyl alcohol and drying them on copper−carbon mesh grids.

3.1. Phase Evolution Studies

To study the phase evolution, we used XRD (Philips X'Pert PRO diffractometer) operated at 30 mA current and 40 kV. The XRD scans were performed in the range from 26–66° with the Cu Kα radiation (wavelength = 0.154 nm) and a scan rate of 0.05°/s. The phase analysis and evolution studies of various phases were done by matching the peaks in the XRD spectrum with the standard international center for diffraction Data- joint committee on powder diffraction standards (ICDD-JCPDS) database using X'pert High Score software provided in the XRD machine. The powder XRD diffraction technique was used to characterize magnetic nanoparticles and to gather basic data on the lattice parameter

and size [49]. The well-known Scherer's equation, $d = \frac{0.89\lambda}{\beta \cos\theta}$ was used to determine the particle size. Here, "d" stands for average crystal size, 0.89 is Scherer's constant, λ is the X-ray wavelength, β is the full width at half-maximum of the diffraction peaks, and θ is the Bragg's diffraction angle. The lattice parameter of Fe_3O_4 and Fe_3O_4@SiO_2 MNPs was calculated from Bragg's law via the Nelson–Riley equation [49].

3.2. Surface Morphology Studies

Advanced transmission electron microscopy (TEM) was used to analyze the size and surface morphology of nanoparticles of each sample. To know surface morphology more deeply, transmission electron microscopy (JEOL-JEM 2100) operating at 20 kV was used. TEM images were acquired in bright field mode. The selected area diffraction patterns were recorded to examine the crystallinity of the produced nanoparticles. ImageJ version 4.0 was used to estimate the nanoparticle size and distribution.

3.3. UV-vis Spectroscopy

UV-vis spectroscopy (UV-vis) was carried out using a UV-vis spectrometer (Agilent Cary 60). The UV-vis diffuse reflectance spectra were recorded with solvent baseline correction in the range of 250 nm to 800 nm and a scanning rate of 24,000 nm min^{-1}.

3.4. FTIR Studies

FTIR studies were performed using a Perkin Elmer Spectrum One with a resolution of 4 cm^{-1}, using a scanning range of 500−4000 cm^{-1} and a scanning rate of 0.20 cm/s.

3.5. Animicrobial Tests

Gram-positive (*Bacillus pumilus*), Gram-negative (*Bacillus halodurons*), and *Candida albicans* fungus were the targets of the antimicrobial testing. The various microbial strains were purchased from the biotechnology lab at SGT University. The microbial bacteria cultures were kept alive at a temperature of 35 ± 2 °C on nutrition Muller-Hinton agar. The bacteria cultures were kept in an appropriate media slant and kept at 51 °C until they were needed. In this study, dimethyl sulfoxide (DMSO) served as the negative control and the all-purpose antibiotic ampicillin served as the positive control. Additionally, Fe_3O_4@SiO_2 was tested for its antibacterial action using a variety of Fe_3O_4 concentrations, and the results were analyzed using a modified version of the agar well disc diffusion method from [30]. We made sterile nutritional plates and gave them a set amount of time to solidify (5 min). Using a chosen borer, 5 mm agar wells were punched in randomly chosen areas of various plates. A homogenous 1 mL inoculum suspension of *Candida albicans*, *Bacillus pumilus*, and *Bacillus halodurons*, as well as Gram-positive and Gram-negative bacteria, was applied to the agar plate surfaces. Furthermore, 15 mL and 20 mL of DMSO were used to solutionize 120 mg of pristine Fe_3O_4 and 150 mg each of Fe_3O_4 and Fe_3O_4@SiO_2 MNPs. As a result, solutions with concentrations of 15 mg/mL and 20 mg/mL were created. The agar well was then filled with 100 L of each prepared MNPs solution. The agar plates were set for overnight incubation at 35 ± 2 °C. Using a millimeter scale, the antimicrobial activity was assessed and recorded in mm with regard to the zone of inhibition. Around the agar well, crystal-clear inhibition zones were seen, which showed the development of the antimicrobial activity.

3.6. Cyclic Voltammetery Studies

Further, the electrochemical sensing of produced MNPs was carried out by using As(III) concentration from (1–10 ppb) by cyclic voltammetry studies. The measurements were conducted with a conventional three-electrode geometry system. The various electrodes used were a working electrode (unmodified or modified), a Ag/AgCl reference electrode saturated with 3 M KCl solution, and a platinum foil electrode as a counter, respectively. The different electrochemical measurements were carried out using Autolab potentiostat PGSTAT 302N (Metrohm Eco Chemie, Utrecht, The Netherlands). The Autolab

machine was provided with the General Purpose Electrochemical Systems software module for data acquisition and analysis (software version 4.9). All the current-potential curves were referred to the AgAgCl reference electrode. The solution pH values were measured with a digital pH meter (model 827, Switzerland make).

4. Results and Discussion

4.1. UV-vis Spectroscopy

Figure 1 shows the UV-vis spectra of Fe_3O_4 and Fe_3O_4@SiO_2 MNPs. Due to a narrow band gap, Fe_3O_4 MNPs exhibit a broad band in the UV and visible spectrum [50]. Fe_3O_4 NPs were used to synthesize Fe_3O_4@SiO_2 MNPs, which resulted in a notable increase in visual absorption. This shows that Fe_3O_4 NPs efficiently increase Fe_3O_4@SiO_2 MNPs ability to absorb visible light due to their well-structured and uniform shell thickness, which may be important for the adsorption of organic dyes from the ambient. Previous studies have shown that the shell thickness of nanoparticles could effectively control the absorbance and antibacterial properties [51]. The visual absorbance dramatically enhanced following the fabrication of the Fe_3O_4@SiO_2 core-shell utilizing Fe_3O_4 NPs.

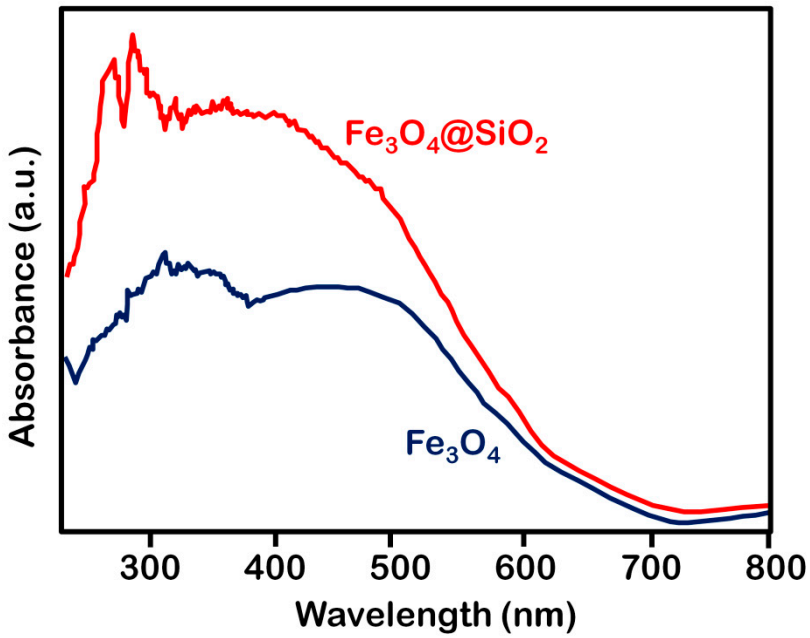

Figure 1. UV-Vis spectra of Fe_3O_4 and Fe_3O_4@SiO_2 MNPs samples.

It was also seen that when the loading amount of Fe_3O_4 increased, the composites' visual absorption gradually increased, and showing Fe_3O_4 could effectively promote visible light absorption. This shows that Fe_3O_4 NPs, which have a well-structured and homogeneous shell thickness, will actively participate in adsorption, as well as substantially increase the visible light absorption of Fe_3O_4@SiO_2. The formation of new peaks around 300 nm in the Fe_3O_4@SiO_2 core-shell are observed. A similar observation is reported by Nazarbady et al. [52], where a new absorbance peak was noticed in the case of 3-methacryloxypropyltrimethoxysilane around the wavelength of 300 nm. The authors attributed this observation to the extension of conjugation brought on by polymerization activity. In the present case, TEOS have been used for the fabrication of Fe_3O_4@SiO_2 MNPs and the peaks observed around 300 nm may be due to similar activity.

4.2. XRD Analysis

Figure 2 shows the XRD patterns of Fe_3O_4 and Fe_3O_4@SiO_2 MNPs. Fe_3O_4 XRD patterns showed sharp peaks, indicating that hydrothermal synthesis was successful in producing pure Fe_3O_4 MNPs. There was no other peak associated with the Fe_3O_4 NPs.

It was discovered that the peaks of Fe_3O_4@SiO_2 MNPs were wider than those of Fe_3O_4 nanostructures. This indicated the refinement of the crystallite size of Fe_3O_4 after the introduction of SiO_2 NPs. The size of Fe_3O_4 NPs does not vary noticeably, but the SiO_2-shell coating increases because of the existing distance between NPs. According to the XRD patterns, magnetite's typical crystal phase matches all of the highly crystalline peaks quite well. The presence of a bumpy peak between 20–30° is assigned to be amorphous SiO_2 [53].

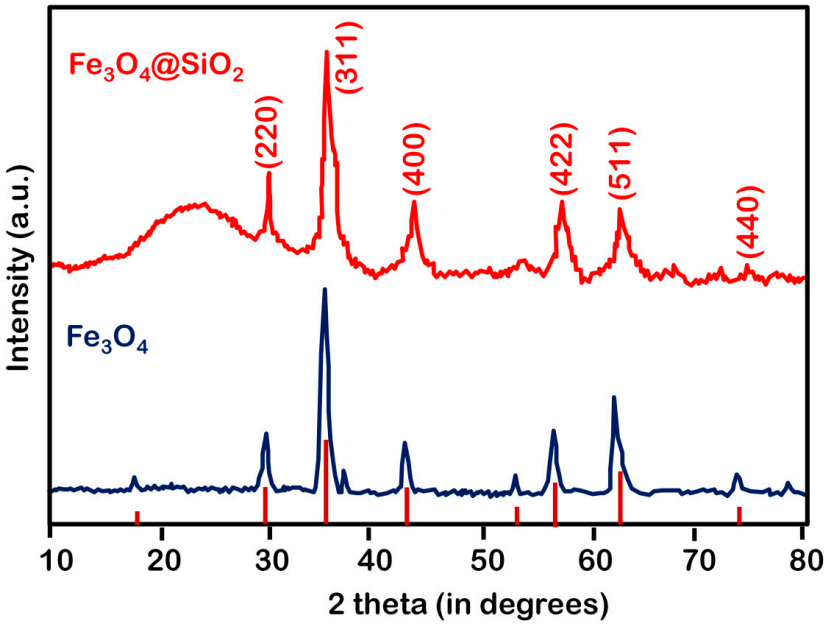

Figure 2. XRD patterns of Fe_3O_4 and Fe_3O_4@SiO_2 MNPs.

The signals produced by Fe_3O_4 nanoparticles were thought to have been decreased by the SiO_2 layer. The fact that the XRD peaks for Fe_3O_4 and Fe_3O_4@SiO_2 MNPs were identical shows that the Fe_3O_4 structure was preserved in the core, where the SiO_2 cover did not affect the crystal structure of the Fe_3O_4 MNPs [54]. The Fe_3O_4 nanoparticle's predicted mean crystallite size was discovered to be 25 ± 5 nm.

The crystal structure of the Fe_3O_4 NPs conforms to a cubic system with lattice parameters and *d*-spacing of 0.29 nm for the miller index of the major peak (311). For the lattice parameter and particle size of Fe_3O_4 NPs generated at varied temperatures, comparable findings were noticed. It was shown that when the temperature increased, both surfactants produced slightly larger NPs, which may be ascribed to the kinetics of agglomeration. The reaction temperature shift for such a method does not favor large particle formation. The mechanisms of growth and nucleation are significantly influenced by temperature. The particle size increases, and the particle size distribution becomes irregular as the temperature rises. Magnetite (Fe_3O_4) is a ferrimagnetic substance with a high Curie temperature of 592 °C among several nanoscale magnetic materials. In the past, navigators employed magnetite, one of the elements studied extensively, to locate the north pole of the earth. Fe_3O_4 loses its magnetic property above 700 °C, hence these materials can only be used below that temperature. For optimal use of ferrite NPs, one must have a thorough understanding of the stability, structure, thermodynamics, and reactivity of iron oxides at high temperatures [55].

As a result, the approach chosen makes it possible to synthesize the material at ambient temperature. It was discovered that both surfactants created slightly larger NPs as the temperature rose, which may be related to the kinetics of agglomeration. Large particle production is not encouraged by the reaction temperature change for such a technique. The temperature has a significant impact on the mechanisms of growth and nucleation [56]. When the temperature rises, the particle size increases, and the particle size distribution become erratic. The kinetic energy of collision increases as a result of an increase in collision

frequencies, which gives nanoparticles a strong tendency to aggregate into larger particles and cross potential barriers between them. The apparent inverse spinel Fe_3O_4 MNPs has diffraction peaks at 30.21°, 35.63°, 43.34°, 53.71°, 57.40°, and 63.11°, which correspond to the orientations of face-centered cubic crystals (220), (311), (400), (422), (511), and (440) planes, respectively [57]. The rest of the peaks are identical to those seen in XRD patterns of Fe_3O_4, and the amorphous character of the peak correlates to SiO_2 materials [46].

4.3. FTIR Analysis

The FTIR analysis of Fe_3O_4 and Fe_3O_4@SiO_2 MNPs is demonstrated in Figure 3. The presence of Fe_3O_4 in the Fe_3O_4@SiO_2 NPs was confirmed by the IR band at 640 cm^{-1} in the Fe_3O_4@SiO_2 spectra, which is caused by the stretching vibration of Fe-O-Fe. This was strengthened even more by the peak's appearance at 1400 cm^{-1}, which was attributed to the stretching vibration of Fe-O-Si. The stretching and bending vibrations of O-Si-O were assigned to the bands at 1102 and 790 cm^{-1} for silica-coated magnetic NPs, respectively [58].

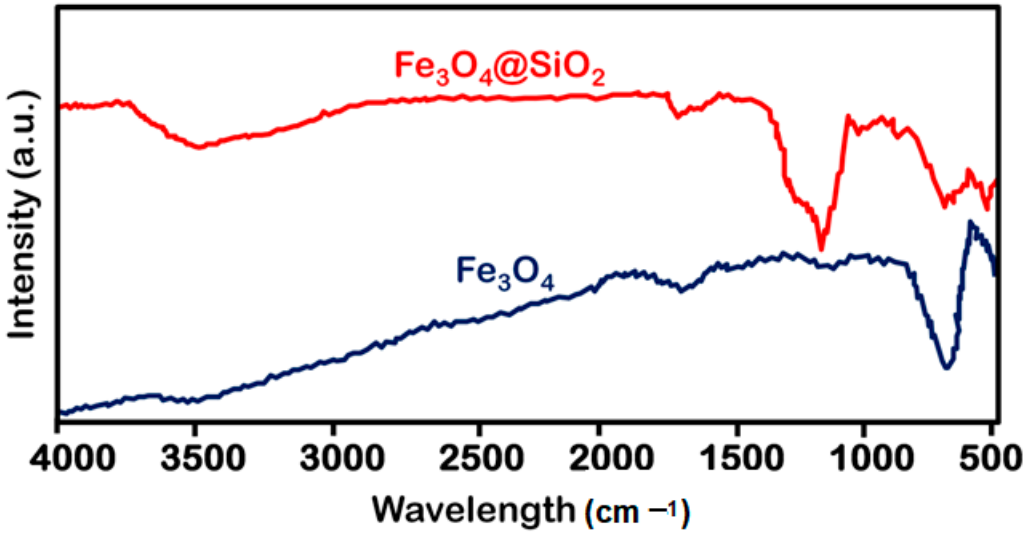

Figure 3. FTIR spectra of Fe_3O_4 NPs and Fe_3O_4@SiO_2 MNPs.

The IR bands, which exhibit the vibrations M_t-O-M_o (600–550 cm^{-1}) and MO-O (440–470 cm^{-1}), respectively, where Mt and Mo represent the metal occupying tetrahedral and octahedral positions, again supported the existence of an inverse spinel type structure for Fe_3O_4 [33]. The presence of OH is shown in Figure 3 by the peaks at 3421 cm^{-1}, which are likely caused by air moisture. The bending vibration of (Si-OH) silanols is well suited to the infrared band at 960 cm^{-1} [58]. Si-O-H stretching vibrations can be assigned the frequency at 1102 cm^{-1} [59]. The signal at 1059 cm^{-1} is attributed to Si-O-Si vibrations, according to the FTIR spectrum of Fe_3O_4@SiO_2 MNPs [60]. The result is consistent with those reported in the past where Alkoxysilanes' 3-aminopropyl amino groups were attached to MNPs [61]. Two strong absorption bands at approximately 636 cm^{-1} and 588 cm^{-1} are indicative of the formation of magnetic nanoparticles. Additionally, the tetrahedral and octahedral sites of the spinel structure may be identified by the absorption bands at 545 cm^{-1} and octahedral sites can be confirmed by the band at 588 cm^{-1} [62].

4.4. Microstructural Analysis using TEM

The morphology and size of Fe_3O_4@SiO_2 MNPs were analyzed by TEM. The typical bright field image of NPs along with the particle size distribution is shown in Figure 4a,b. The bright field image of the Fe_3O_4@SiO_2 MNPs can be seen in Figure 4a. In Figure 4b, the histogram shows the particle size distribution, and the size of the particle varies from 15–30 nm with an average size of 21 nm.

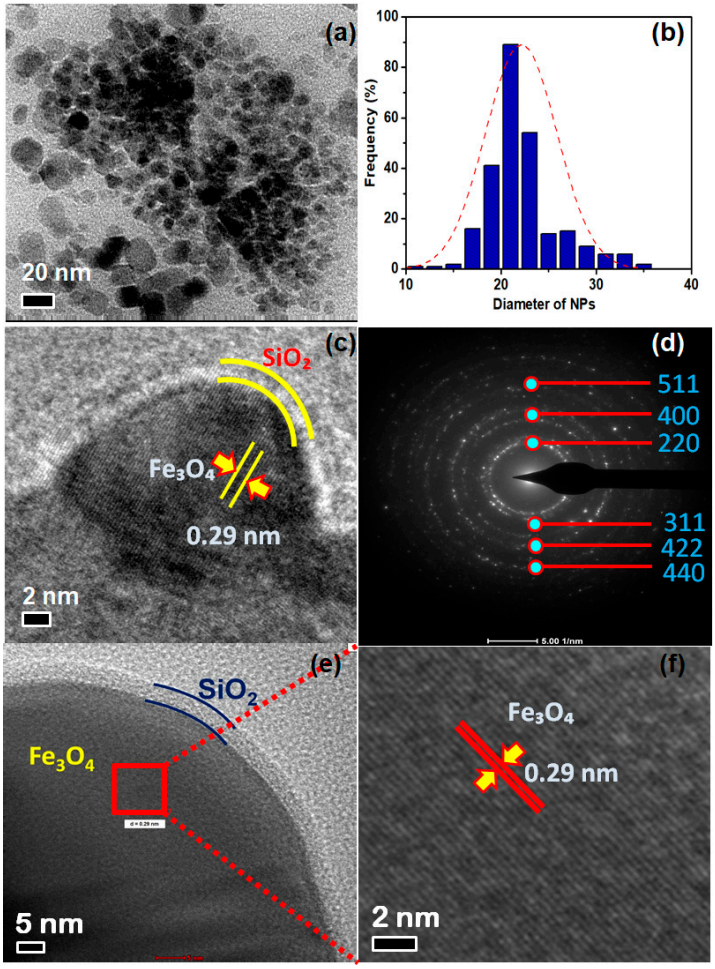

Figure 4. TEM bright field image of (**a**) Fe_3O_4@SiO_2 MNPs with (**b**) size distribution histogram of prepared NPs of 15–20 nm (**c**); (**d**) SAD pattern of Fe_3O_4@SiO_2 MNPs; (**e**,**f**) High-resolution TEM imaging of (**c**).

The high-resolution TEM image shows the core-shell structure of Fe_3O_4@SiO_2 MNPs in Figure 4c. In Figure 4d, the selected area electron diffraction pattern (SAD) shows the different interplanar spacing of (220), (311), (400), (422), (511), and (440) with diffracting conditions and matched well with the XRD pattern, which also confirms that the prepared material is highly polycrystalline. The high-resolution TEM images shown in Figure 4e,f further depict the SiO_2 layer of the Fe_3O_4 core with a thickness of 2 nm. The measured interplanar spacing of the Fe_3O_4 is known to be 0.29 nm corresponding to plane (311) [43,63].

4.5. Antimicrobial Test

Antimicrobial activities of Fe_3O_4 and Fe_3O_4@SiO_2 MNPs examined by the disk diffusion method are illustrated in Figure 5. The test was performed in different cultures of Bacillus pumilus and Bacillus halodurons. The amount of sample had an inhibition zone Fe_3O_4 of 8.5 ±1.0 mm, 12 ± 1.5 mm, 13 ± 1.5 mm, 14 ± 1.0 mm with Fe_3O_4@SiO_2 MNPs 10 ± 1.2 mm, 12.5 ± 1.5 mm, 15 ± 1.0 mm, and 16 ± 1.8 mm with an increase in weight from 5 mg to 20 mg with the step of five in the Bacillus pumilus and Bacillus halodurans culture. Figure 5a,b shows the growth of Gram-positive and Gram-negative bacterial activity on Fe_3O_4@SiO_2 MNPs. The Bacillus pumilus grows in a nourishing environment depleted of SiO_2 in presence of some water activity; moreover, the Bacillus halodurans is a moderate halophilic bacteria. It has been observed that with the increase of SiO_2 concentration, the inhibition zone is also increased. The SiO_2 composited on Fe_3O_4 is a corporal contributory to the repression of the culture of Fe_3O_4 owning to magnetic dipole

interaction. The bond of SiO_2 with the cell membrane in the inhibition zone can alter the structure of bacteria because of attraction in NPs in microbial activity; as a result, there is leakage of cellular content in microbial activity. The presence of SiO_2 on the Fe_3O_4 surface stops the antibacterial activity of MNPs; generally, SiO_2 acts as a molecular link between Fe_3O_4 and microorganisms.

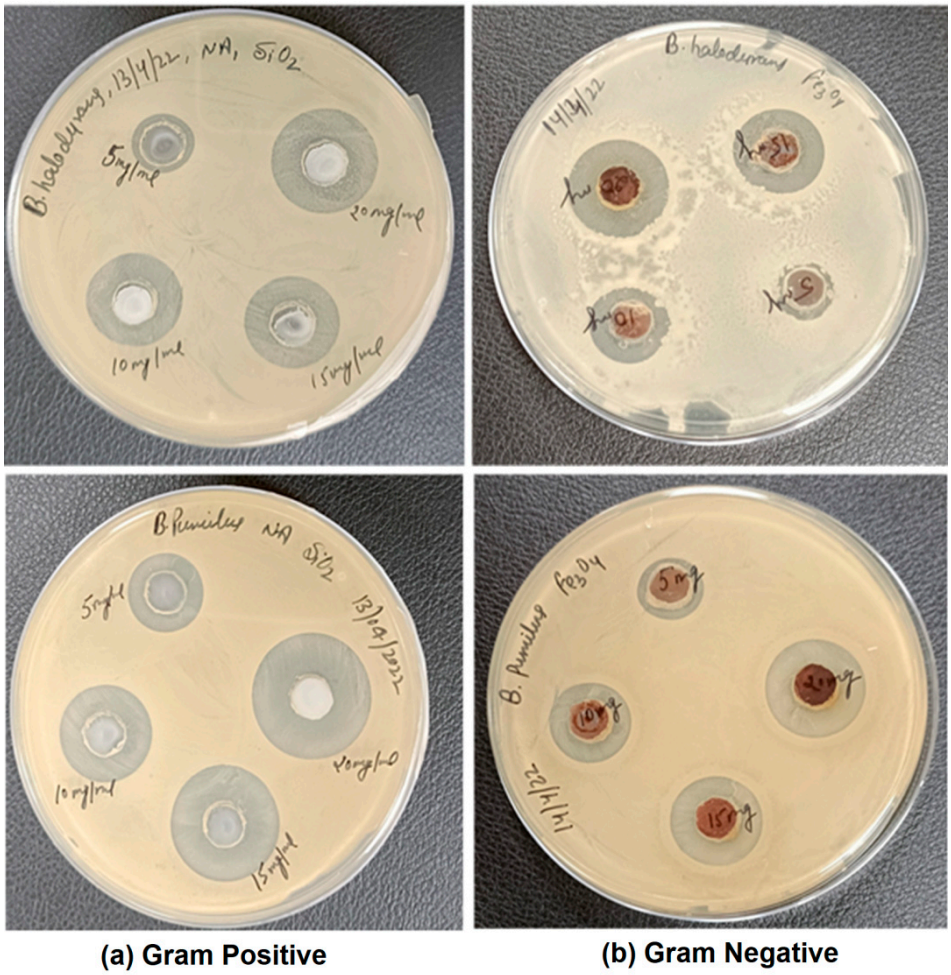

Figure 5. (**a**) Antimicrobial activity on Fe_3O_4 in Bacillus halodurons culture; (**b**) Antimicrobial activities on Fe_3O_4@SiO_2 MNPs in Bacillus pumilus culture.

Previous studies have shown that Gram-positive bacteria have thicker membranes as compared to Gram-negative bacteria, making the former more stable [64]. According to Chen et al., *Escherichia coli* was more susceptible to Fe_3O_4@SiO_2-Ag nanospheres than *Staphylococcus aureus* [64–66]. While Gram-negative bacteria are thin layered with a thickness of 8–10 nm and have a 20–30% lipid content, Gram-positive bacteria are thick layered or single layered with a thickness of 20–80 nm. It has been noted that the inhibitory zone grows along with an increase in SiO_2 concentration. Due to its biocompatibility, biodegradability, and surface-modifiability, Fe_3O_4 is the most promising magnetic material for medical applications [37,38]. In order to separate MNPs in water following antibacterial treatment, Fe_3O_4 superparamagnetic characteristics are mostly advantageous [65]. Additionally, according to Asab et al. [47], Gram-positive bacteria are typically more resistant to Fe_3O_4 NPs than Gram-negative bacteria concerning the composition of their cell walls, cellular physiology, metabolism, or level of interaction [66]. Moreover, Fe_3O_4 is loaded with the SiO_2 NPs in the form of Fe_3O_4@SiO_2 MNPs, which helps in removing the bacteria present over there. The combination of several antibacterial modalities helps in reducing the dosage, increasing efficiency, and reducing side effects [67].

4.6. Cyclic Voltammetry

The electrochemical sensing studies of the Fe_3O_4 and Fe_3O_4@SiO_2 were done by the cyclic voltammetry (CV) curves recorded using the As(III). Figure 6 shows the CV voltammogram response of Fe_3O_4@SiO_2 MNPs and Fe_3O_4@SiO_2 MNPs with varying As(III) concentrations from 1–10 ppb recorded at 10 mVs^{-1} scan rate within the potential window of −0.2–0.8 V. It was seen that with different concentration of As in the solution, CV response curves change their shape and size appreciably. By increasing the concentration of arsenic, there was a shift in potential and an increase in the oxidation peak current, showing the electrocatalytic capacity of the modified electrode. As the pH 6.0 was close to the physiological solutions, the oxidation peak was lower in this study.

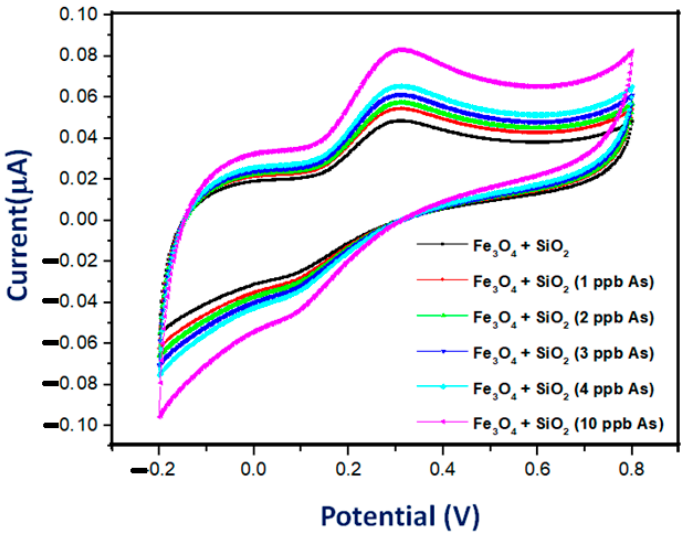

Figure 6. Cyclic voltammetric response of bare Fe_3O_4@SiO_2 MNPs, and Fe_3O_4@SiO_2 MNPs with varying Arsenic concentrations from 1–10 ppb.

The curves of the electrodes trend towards cathodic and anodic peaks back to pseudocapacitive behavior as the redox reactions are established at the electrodes and the reversible reaction between the Fe^{2+}/Fe^{3+} ions of the electrodes and the solution interface [68]. Fe_3O_4@SiO_2 MNPs displayed a well-defined oxidation wave. For Fe_3O_4@SiO_2 MNPs, the oxidation peak potential is noticed at +0.3 V. The anodic peak current response was higher when As(III) concentration was increased from 1 ppb to 10 ppb. The greater accessible surface area of the modified electrode was attributed to the electrocatalytic effect due to the nanoscale dimensions of the sample and the presence of SiO_2, which is essential for electrocatalytic oxidation [69,70].

Furthermore, we notice that the Fe_3O_4@SiO_2 provides a bigger CV response area than that of pristine Fe_3O. This indicates higher capacitive charge storage. The CV response peak of the hybrid Fe_3O_4@SiO_2 was larger than that of the pristine magnetite. Thus, it was inferred that SiO_2 coating enhances the capacitance of Fe_3O_4. At different gravimetric As(III) concentrations, the discharge curves of Fe_3O_4 and Fe_3O_4@SiO_2, and the potential shifted to the negative side gradually as depicted in Figure 6. According to a previous report, the specific capacitance of Fe_3O_4 and Fe_3O_4@SiO_2 samples can be calculated by using the following equation [68]:

$$C_s = \frac{I\Delta t}{m\Delta E}$$

Here, C_s, I, Δt, m, and ΔE are specific capacitance, discharge current, discharge time, the active mass of electrodes, and IR discharge drops. According to these findings, the specific capacitance of these prepared electrodes appears to fall as the current densities increase. This observation shows the pseudocapacitive behavior with favorable electrochemical sensing characteristics. A reduced specific capacitance can be attributed to the

increase in current that reduces the discharge time of ions needed to enter through the electrodes. Additionally, these observations support the fact that the discharge time is reducing as the current density rises, signifying an increase in the drop voltage. The specific capacitance of Fe_3O_4 and Fe_3O_4@SiO_2 modified electrodes, calculated according to the above equation, were 166 and 201 A/g, respectively, at the charge current of 10 A/g. This shows that the SiO_2 coating on the Fe_3O_4 electrode is increasing the specific capacitance by enhancing the nucleation sites for energy storage. Therefore, the coating of SiO_2 to Fe_3O_4 offers significant electron transport on and within Fe_3O. All of these phenomena have led to the improvement of the electrodes for electrochemical sensing and reduced electrode resistance [71].

5. Conclusions

1. The solvothermal approach has been used to successfully create Fe_3O_4 NPs coated with SiO_2 NPs. The XRD, UV-vis, and FTIR results demonstrate the creation of spinal Fe_3O_4@SiO_2 structure. A thorough examination of the TEM reveals the formation of Fe_3O_4 cell structure. Additionally, the size distribution of Fe_3O_4@SiO_2 MNP size distribution ranges from 10 to 30 nm.
2. The antimicrobial tests showed a larger inhibition zone of Fe_3O_4 coated by SiO_2 as compared to the pure Fe_3O_4 NPs. Fe_3O_4@SiO_2 MNPs showed strong antibacterial characteristics by killing bacteria on the exterior, as well as inside, of their cell membranes.
3. The electrochemical sensor based on Fe_3O_4 coated with SiO_2 NPs is capable of reducing and oxidizing arsenic with outstanding electrocatalytic activity. Fe_3O_4 covered with SiO_2 naturally enhances the sensitivity of the determination of arsenic (III) with a low detection limit because of its distinctive qualities, which include subtle electrical characteristics, good interaction, and strong adsorptive capacity.
4. Varying the arsenic content resulted in a shift in potential and an increase in the oxidation peak current, which illustrates the improved electrode's electrocatalytic capability.
5. It was concluded that the combination of SiO_2 with the Fe_3O_4 NPs improves the antibacterial property of Fe_3O_4 and reduces the adverse effects. Additionally, the composite Fe_3O_4@SiO_2 can be used against bacteria as well as for the detection of arsenic pollutants as an electrochemical sensor.

Author Contributions: Conceptualization, M.K. and J.R.A.; methodology, M.; formal analysis, V.K. and S.N.; investigation, J.R.A., S.N., A.S.; writing—original draft preparation, M. and J.R.A.; writing—review and editing, M.K. and A.S.; supervision, M.K. and A.S.; project administration, A.S. and M.K.; funding acquisition, A.S. All authors have read and agreed to the published version of the manuscript.

Funding: This research received no external funding.

Institutional Review Board Statement: Not applicable.

Informed Consent Statement: Not Applicable.

Data Availability Statement: The data used to support the findings of this study are available from the corresponding author upon request.

Acknowledgments: The authors are thankful to the Department of Material Science and Engineering, Indian Institute of Technology, Delhi for the help in XRD characterizations. The authors are also grateful to the SAIF, AIIMS, New Delhi, India for carrying out the TEM characterizations. MK and JRA are also thankful to Shree Guru Gobind Singh Tricentenary University Gurugram and LIET, Alwar for their support for this work.

Conflicts of Interest: The authors declare no conflict of interest.

References

1. Wang, Y.; Ding, X.; Chen, Y.; Guo, M.; Zhang, Y.; Guo, X.; Gu, H. Antibiotic-loaded, silver core-embedded mesoporous silica nano-vehicles as a synergistic antibacterial agent for the treatment of drug-resistant infections. *Biomaterials* **2016**, *101*, 207–216. [CrossRef] [PubMed]
2. Neu, H.C. The crisis in antibiotic resistance. *Science* **1992**, *257*, 1064–1073. [CrossRef] [PubMed]
3. Ackermann-Liebrich, U.A.; Nocera, S.; Merten, S. A solution for creating competent health-care specialists: The Swiss School of Public Health. *Bull. World Health Organ.* **2007**, *85*, 974–976. [CrossRef] [PubMed]
4. You, Q.; Zhang, X.; Wu, F.G.; Chen, Y. Colorimetric and test stripe-based assay of bacteria by using vancomycin-modified gold nanoparticles. *Sens. Actuators B Chem.* **2019**, *281*, 408–414. [CrossRef]
5. Wang, C.; Zhang, K.; Zhou, Z.; Li, Q.; Shao, L.; Hao, R.Z.; Xiao, R.; Wang, S. Vancomycin-modified Fe_3O_4@SiO_2@Ag microflowers as effective antimicrobial agents. *Int. J. Nanomed.* **2017**, *12*, 3077–3094. [CrossRef]
6. Morens, D.M.; Folkers, G.K.; Fauci, A.S. The challenge of emerging and re-emerging infectious diseases. *Nature* **2004**, *430*, 242–249. [CrossRef]
7. Xu, J.; Zhao, Q.; Hu, T.; Chen, X.; Cao, Y. Rapid preparation of size-tunable Fe_3O_4@SiO_2 nanoparticles to construct magnetically responsive photonic crystals. *J. Nanopart. Res.* **2021**, *23*, 232. [CrossRef]
8. Tzounis, L.; Logothetidis, S. Fe_3O_4@SiO_2 core shell particles as platforms for the decoration of Ag nanoparticles. *Mater. Today Proc.* **2017**, *4*, 7076–7082. [CrossRef]
9. Quirós, J.; Boltes, K.; Aguado, S.; de Villoria, R.G.; Vilatela, J.J.; Rosal, R. Antimicrobial metal–organic frameworks incorporated into electrospun fibers. *Chem. Eng. J.* **2015**, *262*, 189–197. [CrossRef]
10. Tan, P.; Li, Y.H.; Liu, X.Q.; Jiang, Y.; Sun, L.B. Core–shell AgCl@SiO_2 nanoparticles: Ag(I)-based antibacterial materials with enhanced stability. *ACS Sustain. Chem. Eng.* **2016**, *4*, 3268–3275. [CrossRef]
11. Zhang, X.; Niu, H.; Yan, J.; Cai, Y. Immobilizing silver nanoparticles onto the surface of magnetic silica composite to prepare magnetic disinfectant with enhanced stability and antibacterial activity. *Colloid. Surf. A Physicochem. Eng. Asp.* **2011**, *375*, 186–192. [CrossRef]
12. Zheng, K.; Setyawati, M.I.; Lim, T.P.; Leong, D.T.; Xie, J. Antimicrobial cluster bombs: Silver nanoclusters packed with daptomycin. *ACS Nano* **2016**, *10*, 7934–7942. [CrossRef] [PubMed]
13. Miyazawa, N.; Hakamada, M.; Mabuchi, M. Antimicrobial mechanisms due to hyperpolarisation induced by nanoporous Au. *Sci. Rep.* **2018**, *8*, 3870. [CrossRef] [PubMed]
14. Sadighian, S.; Sharifan, K.; Khanmohammadi, A.; Rohani, M.K. A facile synthesis of Fe_3O_4@SiO_2@ZnO for Curcumin delivery. *Biointerface Res. Appl. Chem.* **2021**, *12*, 7994–8002. [CrossRef]
15. Kim, Y.H.; Lee, D.K.; Cha, H.G.; Kim, C.W.; Kang, Y.C.; Kang, Y.S. Preparation and characterization of the antibacterial Cu nanoparticle formed on the surface of SiO_2 nanoparticles. *J. Phys. Chem. B* **2006**, *110*, 24923–24928. [CrossRef]
16. Lei, S.; Zhao, H.; Pang, B.; Qu, R.; Lian, Z.; Jiang, C.; Shao, D.; Huang, Q.; Jin, M.; Shi, J. Capability of iturin from Bacillus subtilis to inhibit Candida albicans in vitro and in vivo. *Appl. Microbiol. Biotechnol.* **2019**, *103*, 4377–4392. [CrossRef]
17. Li, Y.; Wang, X.Y.; Jiang, X.P.; Ye, J.J.; Zhang, Y.W.; Zhang, X.Y. Fabrication of graphene oxide decorated with Fe_3O_4@SiO_2 for immobilization of cellulose. *J. Nanopart. Res.* **2015**, *17*, 8. [CrossRef]
18. Babay, S.; Mhiri, T.; Toumi, M. Synthesis, structural and spectroscopic characterizations of maghemite γ-Fe_2O_3 prepared by one-step coprecipitation route. *J. Mol. Struct.* **2015**, *1085*, 286–293. [CrossRef]
19. Akbarzadeh, A.; Samiei, M.; Davaran, S. Magnetic nanoparticles: Preparation, physical properties, and applications in biomedicine. *Nanoscale Res. Lett.* **2012**, *7*, 144. [CrossRef]
20. Wu, W.; He, Q.; Jiang, C. Magnetic iron oxide nanoparticles: Synthesis and surface functionalization strategies. *Nanoscale Res. Lett.* **2008**, *3*, 397. [CrossRef]
21. Tchounwou, P.B.; Yedjou, C.G.; Patlolla, A.K.; Sutton, D.J. Heavy Metals Toxicity and the Environment. In *Molecular, Clinical and Environmental Toxicology. Experientia Supplementum*; Luch, A., Ed.; Springer: Basel, Switzerland, 2012; Volume 101.
22. Hajipour, P.; Eslami, A.; Bahrami, A.; Hosseini-Abari, A.; Saber, F.Y.; Mohammadi, R.; Mehr, M.Y. Surface modification of TiO_2 nanoparticles with CuO for visible-light antibacterial applications and photocatalytic degradation of antibiotics. *Ceram. Int.* **2021**, *47*, 33875–33885. [CrossRef]
23. Beitollahi, H.; Nejad, F.G.; Shakeric, S. GO/Fe_3O_4@SiO_2 core–shell nanocomposite modified graphite screen-printed electrode for sensitive and selective electrochemical sensing of dopamine and uric acid. *Anal. Methods* **2017**, *9*, 5541. [CrossRef]
24. Shi, G.; Sun, B.; Jin, Z.; Liu, Z.; Li, M. Synthesis of SiO_2/Fe_3O_4 nanomaterial and its application as cataluminescence gas sensor material for ether. *Sens. Actuators B* **2012**, *171–172*, 699–704. [CrossRef]
25. Ansari, J.R.; Naseh, M.F.; Singh, N.; Sarkar, T.; Datta, A. Unique photoluminescence response of MoS_2 quantum dots over a wide range of As (III) in aqueous media. *Nanotechnology* **2021**, *32*, 345708. [CrossRef] [PubMed]
26. Prucek, R.; Tuček, J.; Kilianová, M.; Panáček, A.; Kvítek, L.; Filip, J.; Kolář, M.; Tománková, K.; Zbořil, R. The targeted antibacterial and antifungal properties of magnetic nanocomposite of iron oxide and silver nanoparticles. *Biomaterials* **2011**, *32*, 4704–4713. [CrossRef]
27. Qu, M.; Chen, Z.; Sun, Z.; Zhou, D.; Xu, W.; Tang, H.; Gu, H.; Liang, T.; Hu, P.; Li, G.; et al. Rational design of asymmetric atomic Ni-P_1N_3 active sites for promoting electrochemical CO reduction. *Nano Res.* 2022, in press. [CrossRef]

28. Huo, J.; Wei, H.; Fu, L.; Zhao, C.; He, C. Highly active $Fe_{36}Co_{44}$ bimetallic nanoclusters catalysts for hydrolysis of ammonia borane: The first-principles study. *Chin. Chem. Lett.* 2022, in press. [CrossRef]
29. Ghasemzadeh, M.A.; Abdollahi-Basir, M.H.; Babaei, M. Fe_3O_4@SiO_2–NH_2 core-shell nanocomposite as an efficient and green catalyst for the multi-component synthesis of highly substituted chromeno[2,3-b]pyridines in aqueous ethanol media. *Green Chem. Lett. Rev.* **2015**, *8*, 40–49. [CrossRef]
30. Prasad, K.; Lekshmi, G.S.; Ostrikov, K.; Lussini, V.; Blinco, J.; Mohandas, M.; Vasilev, K.; Bottle, S.; Bazaka, K.; Ostrikov, K. Synergic bactericidal effects of reduced graphene oxide and silver nanoparticles against Gram-positive and Gram-negative bacteria. *Sci. Rep.* **2017**, *7*, 1591. [CrossRef]
31. Cong, Y.; Xia, T.; Zou, M.; Li, Z.; Peng, B.; Guo, D.; Deng, Z. Mussel-inspired polydopamine coating as a versatile platform for synthesizing polystyrene/Ag nanocomposite particles with enhanced antibacterial activities. *J. Mater. Chem. B* **2014**, *2*, 3450–3461. [CrossRef]
32. Liu, L.; Yang, J.; Xie, J.; Luo, Z.; Jiang, J.; Yang, Y.Y.; Liu, S. The potent antimicrobial properties of cell penetrating peptide-conjugated silver nanoparticles with excellent selectivity for Gram-positive bacteria over erythrocytes. *Nanoscale* **2013**, *5*, 3834. [CrossRef] [PubMed]
33. Lu, Y.; Yin, Y.; Mayers, B.T.; Xia, Y. Modifying the surface properties of superparamagnetic iron oxide nanoparticles through a sol−gel approach. *Nano Lett.* **2002**, *2*, 183–186. [CrossRef]
34. Habila, M.A.; Alothman, Z.A.; El-Toni, A.M.; Labis, J.P.; Soylak, M. Synthesis and application of Fe_3O_4@SiO_2@TiO_2 for photocatalytic decomposition of organic matrix simultaneously with magnetic solid phase extraction of heavy metals prior to ICP-MS analysis. *Talanta* **2016**, *154*, 539–547. [CrossRef] [PubMed]
35. Wegmann, M.; Scharr, M. Synthesis of magnetic iron oxide nanoparticles. In *Precision Medicine*; Elsevier: Amsterdam, The Netherlands, 2018; pp. 145–181. [CrossRef]
36. Mukherjee, S.; Chowdhury, D.; Kotcherlakota, R.; Patra, S.; Vinothkumar, B.; Bhadra, M.P.; Sreedhar, B.; Patra, C.R. Potential theranostics application of bio-synthesized silver nanoparticles (4-in-1 System). *Theranostics* **2014**, *4*, 316–335. [CrossRef]
37. Hui, C.; Shen, C.; Tian, J.; Bao, L.; Ding, H.; Li, C.; Tian, Y.; Shi, X.; Gao, H.-J. Core-shell Fe_3O_4@SiO_2 nanoparticles synthesized with well-dispersed hydrophilic Fe_3O_4 seeds. *Nanoscale* **2011**, *3*, 701–705. [CrossRef]
38. Liu, M.C.; Liu, B.; Sun, X.Y.; Lin, H.C.; Lu, J.Z.; Jin, S.F.; Yan, S.Q.; Li, Y.Y.; Zhao, P. Core/shell structured Fe_3O_4@TiO_2 -DNM nanospheres as multifunctional anticancer platform: Chemotherapy and photodynamic therapy research. *J. Nanosci. Nanotechnol.* **2018**, *18*, 4445–4456. [CrossRef]
39. Bharadishettar, N.; Udaya, B.K.; Panemangalore, D.B. Coating Technologies for Copper Based Antimicrobial Active Surfaces: A Perspective Review. *Metals* **2021**, *11*, 711. [CrossRef]
40. Gaviria, J.; Alcudia, A.; Begines, B.; Beltrán, A.M.; Rodríguez-Ortiz, J.A.; Trueba, P.; Villarraga, J.; Torres, Y. Biofunctionalization of Porous Ti Substrates Coated with Ag Nanoparticles for Potential Antibacterial Behavior. *Metals* **2021**, *11*, 692. [CrossRef]
41. Frida, E.; Bukit, N.; Bukit, F.R.A.; Bukit, B.F. Preparation and characterization of Bentonite-OPBA nanocomposite as filler. *J. Phys. Conf. Ser.* **2022**, *2165*, 012023. [CrossRef]
42. Wang, S.; Tang, J.; Zhao, H.; Wan, J.; Chen, K. Synthesis of magnetite–silica core–shell nanoparticles via direct silicon oxidation. *J. Colloid Interf. Sci.* **2014**, *432*, 43–46. [CrossRef]
43. Qu, H.; Tong, S.; Song, K.; Ma, H.; Bao, G.; Pincus, S.; Zhou, W.; O'Connor, C. Controllable in situ synthesis of magnetite coated silica-core water-dispersible hybrid nanomaterials. *Langmuir* **2013**, *29*, 10573–10578. [CrossRef] [PubMed]
44. Sandler, S.E.; Fellows, B.; Mefford, O.T. Best practices for characterization of magnetic nanoparticles for biomedical applications. *Anal. Chem.* **2019**, *91*, 14159–14169. [CrossRef] [PubMed]
45. Qiao, L.; Liu, Z.; Zhang, S. Magnetic solid acid Fe_3O_4@SiO_2-SO_3H for cellulose hydrolysis. *Biomass Conv. Bioref.* **2021**, 1–8. [CrossRef]
46. Shao, D.; Lu, M.; Zhao, Y.; Zhang, F.; Tan, Y.; Zheng, X.; Pan, Y.; Xiao, X.; Wang, Z.; Dong, W.; et al. The shape effect of magnetic mesoporous silica nanoparticles on endocytosis, biocompatibility and biodistribution. *Acta Biomater.* **2017**, *49*, 531–540. [CrossRef] [PubMed]
47. Asab, G.; Zereffa, E.A.; Abdo Seghne, T. Synthesis of silica-coated Fe_3O_4 nanoparticles by microemulsion method: Characterization and evaluation of antimicrobial activity. *Int. J. Biomater.* **2020**, *2020*, 4783612. [CrossRef] [PubMed]
48. Stöber, W.; Fink, A.; Bohn, E. Controlled growth of monodisperse silica spheres in the micron size range. *J. Colloid Inter. Sci.* **1968**, *26*, 62–69. [CrossRef]
49. Cullity, B.D.; Stock, S.R. *Elements of X-ray Diffraction*, 3rd ed.; Prentice-Hall, Inc.: Hoboken, NJ, USA, 2001.
50. Cao, Y.; Li, C.; Li, J.; Li, Q.; Yang, J. Magnetically separable Fe_3O_4/AgBr hybrid materials: Highly efficient photocatalytic activity and good stability. *Nanoscale Res. Lett.* **2015**, *10*, 251. [CrossRef]
51. Sosiati, H.; Budi, S.; Alaydrus, M.; Handoko, E. Microwave absorbing characteristics of Fe_3O_4@SiO_2 core–shell polyaniline-based composites. *Mater. Res. Express* **2021**, *8*, 046101.
52. Nazarabady, M.M.; Farzi, G. The effect of tunable morphology on the potential application of p(acrylic acid-co-2-ethylhexyl acrylate)/silica nanohybrids. *e-Polymers* **2017**, *17*, 471–480. [CrossRef]
53. Subhan, F.; Aslam, S.; Yan, Z.; Khan, M.; Etim, U.J.; Naeem, M. Effective adsorptive performance of Fe_3O_4@SiO_2 core shell spheres for methylene blue: Kinetics, isotherm and mechanism. *J. Porous Mater.* **2019**, *26*, 1465–1474. [CrossRef]

54. Mirzabe, G.H.; Keshtkar, A.R. Application of response surface methodology for thorium adsorption on PVA/Fe_3O_4/SiO_2/APTES nanohybrid adsorbent. *J. Ind. Eng. Chem.* **2015**, *26*, 277–285. [CrossRef]
55. Ayyappan, S.; Panneerselvam, G.; Antony, M.P.; Rama Rao, N.V.; Thirumurugan, N.; Bharathi, A.; Philip, J. Effect of initial particle size on phase transformation temperature of surfactant capped Fe_3O_4 nanoparticles. *J. Appl. Phys.* **2011**, *109*, 084303. [CrossRef]
56. Cai, W.; Wan, J. Facile synthesis of superparamagnetic magnetite nanoparticles in liquid polyols. *J. Colloid Interf. Sci.* **2007**, *305*, 366–370. [CrossRef] [PubMed]
57. Hong, R.Y.; Zhang, S.Z.; Di, G.Q.; Li, H.Z.; Zheng, Y.; Ding, J.; Wei, D.G. Preparation, characterization and application of Fe_3O_4/ZnO core/shell magnetic nanoparticles. *Mater. Res. Bull.* **2008**, *43*, 2457–2468. [CrossRef]
58. Sadeghi, S.; Azhdari, H.; Arabi, H.; Moghaddam, A.Z. Surface modified magnetic Fe_3O_4 nanoparticles as a selective sorbent for solid phase extraction of uranyl ions from water samples. *J. Hazard. Mater.* **2012**, *215–216*, 208–216. [CrossRef]
59. Zhao, Y.; Li, J.; Zhao, L.; Zhang, S.; Huang, Y.; Wu, X.; Wang, X. Synthesis of amidoxime-functionalized Fe_3O_4@SiO_2 core–shell magnetic microspheres for highly efficient sorption of U(VI). *Chem. Eng. J.* **2014**, *235*, 275–283. [CrossRef]
60. Maboudi, S.A.; Shojaosadati, S.A.; Arpanaei, A. Synthesis and characterization of multilayered nanobiohybrid magnetic particles for biomedical applications. *Mater. Des.* **2017**, *115*, 317–324. [CrossRef]
61. Bini, R.A.; Marques, R.F.C.; Santos, F.J.; Chaker, J.A.; Jafelicci, M. Synthesis and functionalization of magnetite nanoparticles with different amino-functional alkoxysilanes. *J. Magn. Magn. Mater.* **2012**, *324*, 534–539. [CrossRef]
62. Prabhu, Y.T.; Rao, K.V.; Kumari, B.S.; Kumar, V.S.S.; Pavani, T. Synthesis of Fe_3O_4 nanoparticles and its antibacterial application. *Int. Nano Lett.* **2015**, *5*, 85–92. [CrossRef]
63. Kim, B.H.; Yang, J.; Lee, D.; Choi, B.K.; Hyeon, T.; Park, J. Liquid-phase transmission electron microscopy for studying colloidal inorganic nanoparticles. *Adv. Mater.* **2018**, *30*, 1703316. [CrossRef]
64. Chen, S.S.; Xu, H.; Xu, H.J.; Yu, G.J.; Gong, X.L.; Fang, Q.L.; Leung, K.C.F.; Xuan, S.H.; Xiong, Q.R. A facile ultrasonication assisted method for Fe_3O_4@SiO_2-Ag nanospheres with excellent antibacterial activity. *Dalton Trans.* **2015**, *44*, 9140–9148. [CrossRef]
65. Gong, P.; Li, H.; He, X.; Wang, K.; Hu, J.; Tan, W.; Zhang, S.; Yang, X. Preparation and antibacterial activity of Fe_3O_4@Ag nanoparticles. *Nanotechnology* **2007**, *18*, 285604. [CrossRef]
66. Reddy, K.M.; Feris, K.; Bell, J.; Wingett, D.G.; Hanley, C.; Punnoose, A. Selective toxicity of zinc oxide nanoparticles to prokaryotic and eukaryotic systems. *Appl. Phys. Lett.* **2007**, *90*, 213902. [CrossRef] [PubMed]
67. Yu, N.; Cai, T.; Sun, Y.; Jiang, C.; Xiong, H.; Li, Y.; Peng, H. A novel antibacterial agent based on AgNPs and Fe_3O_4 loaded chitin microspheres with peroxidase-like activity for synergistic antibacterial activity and wound-healing. *Int. J. Pharmaceut.* **2018**, *552*, 277–287. [CrossRef] [PubMed]
68. Mustafa, M.A.; Qasim, Q.A.; Mahdi, A.B.; Izzat, S.E.; Alnassar, Y.S.; Abood, E.S.; Alhakim, Z.J.; Mahmoud, Z.H.; Rheima, A.M.; Al-Salman, H.N.K. Supercapacitor performance of Fe_3O_4 and Fe_3O_4@SiO_2-bis(aminopyridine)-Cu hybrid nanocomposite. *Int. J. Electrochem. Sci.* **2022**, *17*, 221057. [CrossRef]
69. Suresh, R.; Giriabu, K.; Manigandan, R.; Vijayalakshmi, L.; Stephen, A.; Narayanan, V. Electrochemical sensing behaviour of Ni doped Fe_3O_4 nanoparticles. *AIP Conf. Proc.* **2014**, *1576*, 122. [CrossRef]
70. Vatandost, E.; Ghorbani-Hasan Saraei, A.; Chekin, F.; Raeisi, S.N.; Shahidi, S.A. Electrochemical sensor based on magnetic Fe_3O_4–reduced graphene oxide hybrid for sensitive detection of Binaphthol. *Russ. J. Electrochem.* **2021**, *57*, 490–498. [CrossRef]
71. Lee, K.S.; Seo, Y.J.; Jeong, H.T. Capacitive behavior of functionalized activated carbon-based all-solid-state supercapacitor. *Carbon Lett.* **2021**, *31*, 1041–1049. [CrossRef]